CRYSTAL GROWTH & DESIGN

pubs.acs.org/crystal

Article

Piracetam and Oxiracetam Afford Molecular, Cocrystalline, and Ionic Cocrystalline Solid Solutions

Published as part of Crystal Growth & Design special issue "Multi-Component Pharmaceutical Solids".

Enrico Spoletti, Ting Wen, Fucheng Leng, Nathan Boukioud, Jason Carty Lacey, Shaza Darwish, Oleksii Shemchuk, Koen Robeyns, Tom Leyssens,* and Matteo Lusi*

Cite This: *Cryst. Growth Des.* 2025, 25, 6754−6763

Read Online

ACCESS | Metrics & More | Article Recommendations | Supporting Information

ABSTRACT: Solid solutions (SSs) are relatively underexplored crystalline forms that allow precise dosage of multidrug formulations. The cocrystallization of the nootropic drugs Piracetam (PIR) and Oxiracetam (OXI) suggests that these phases have a richer scope than once thought. Despite their different H-bond capabilities, multiple solid solutions were obtained following a crystal engineering approach. A combination of the pure compounds produced multiple forms of $PIR_xRS\text{-}OXI_{1-x}$ SS, whose structure depends on the PIR/OXI ratio. Such structural diversity is controlled when enantiopure S-OXI is used in $PIR_xS\text{-}OXI_{1-x}$, or when both drugs are cocrystallized with either a molecular coformer (gallic acid, GA) or an inorganic salt ($MgCl_2$) to produce cocrystalline (CC) and ionic cocrystalline (ICC) SS: $PIR_x{\cdot}RS\text{-}OXI_{1-x}{\cdot}GA$, $PIR_x{\cdot}S\text{-}OXI_{1-x}{\cdot}GA$, and $PIR_xR/S\text{-}OXI_{1-x}{\cdot}MgCl_2{\cdot}5H_2O$. Thermal and humidity stability of each form is discussed, as well as the solubility profile of the GA CCSS. Overall, a rich solid-form landscape has been demonstrated for the combined drugs that allows for designing and optimizing them into molecular, cocrystalline, and ionic cocrystalline solid solutions.

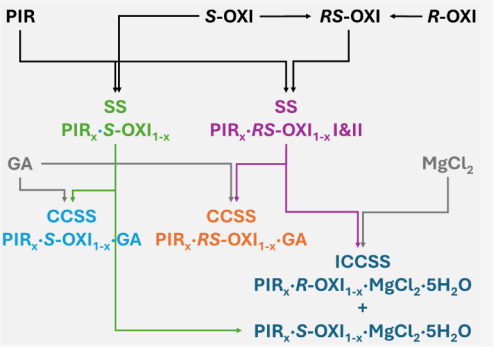

INTRODUCTION

In recent years, multicomponent crystals have attracted growing attention in the pharmaceutical industry as a means for improving important physicochemical properties of solid drug forms, including dissolution rate, thermal stability, morphology, hygroscopicity, and compressibility.[1−4] Furthermore, the cocrystallization of two or more active pharmaceutical ingredients (APIs) with synergistic or complementary therapeutic effect in a single phase has become a convenient strategy to develop fixed-dose combination drugs (FDC). Such drug−drug cocrystals[5−7] offer the chance of simpler administration and better patients' compliance.[8−11] However, in many cases, the fixed stoichiometry of these forms may limit their clinical application.[12] In this view, pharmaceutical solid solutions (SSs) would allow the variation of the APIs' stoichiometry in continuum,[13,14] which translates into dosage flexibility for personalized therapies.

Unfortunately, drug−drug SSs are rather uncommon[15,16] because they require two components with similar chemical structures and the ability to form analogous supramolecular interactions within the crystal.[17] In practice, solid-state soluble components usually differ in a single functional group with similar size and supramolecular capabilities, for example, hydrogen/fluorine, chlorine/bromine, and hydroxyl/amine.[15,16,18−21] Complete solubility, which often involves a pair of molecules that can crystallize in isomorphous or isostructural forms,[14,22,23] is even rarer and represents the main obstacle for the widespread use of pharmaceutical solid solutions. However, sometimes solid-state solubility can be increased by the addition of a third compound, as in salts and cocrystals, or in network materials such as coordination polymers.[24−28] Apart from some recent examples, the crystallographic landscape of solid solutions has been seen as predictable, with one of two forms that change regularly with composition, which limits their structural (and property) diversity.[14,29]

This work reports the attempts to obtain drug−drug SSs between piracetam (PIR) and oxiracetam (both the racemate RS-OXI and the enantiopure S-OXI), two nootropic drugs of the racetam family that differ in a −H/−OH group (Chart 1). In addition to a possible synergistic effect of the two APIs, a solid solution demonstrates the mutual solubility in the solid state of two molecules with different H-bonding capabilities.[30]

Received: May 21, 2025
Revised: July 11, 2025
Accepted: July 14, 2025
Published: July 30, 2025

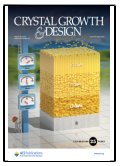

https://doi.org/10.1021/acs.cgd.5c00735
Cryst. Growth Des. 2025, 25, 6754−6763

Chart 1. Chemical Structures of Piracetam (left), RS-Oxiracetam (Middle), and S-Oxiracetam (Right)

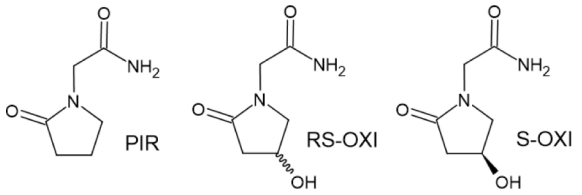

Two cocrystalline solid solutions (CCSSs) were also produced by introducing either an inorganic salt, $MgCl_2$, or an organic coformer, gallic acid (GA). Both are safe pharmaceutical ingredients (GRAS), known to form cocrystals with racetams,[31−33] and might complement the treatment of cognitive deficits and neurodegenerative diseases.[34,35]

EXPERIMENTAL SECTION

Piracetam (PIR) was obtained from UCB Pharma S.A. (mixture of form II and form III) and from Xiamen Top Health Biochem Tech. Co. Ltd. (form III); RS-oxiracetam (RS-OXI) was purchased from Xiamen Top Health Biochem Tech. Co. Ltd.; and S-oxiracetam (S-OXI) was purchased from BLD Pharmatech Ltd.; $MgCl_2$ purchased from Sigma-Aldrich; anhydrous gallic acid (GA form II) was obtained by dehydrating the monohydrate form, which was purchased from Sigma-Aldrich, in an oven at 120 °C overnight. Reagents were used without further purification. All experimental details are given in the Supporting Information section.

Liquid-Assisted Grinding (LAG). LAG was performed by manual grinding of the reagents in the desired stoichiometric ratios with an agate mortar and pestle, in the presence of a small amount of solvent (a few drops; one drop ≈40 μL). LAG was also performed by kneading the reagents in the presence of a small amount of solvent in a Retsch MM400 ball miller operated at a frequency of 25 Hz (5 mL agate jar, with one agate ball 10 mm in diameter). See the Supporting Information for details.

Solution Growth of Single Crystals. *SS $PIR_xRS\text{-}OXI_{1-x}$.* 100 mg of the mixture of PIR and RS-OXI was prepared in the desired stoichiometric ratios (30:70, 50:50) and dissolved in ≈2 mL of water in a vial. Additionally, equimolar solutions of PIR and RS-OXI in methanol were mixed in a vial corresponding to a stoichiometric ratio of 53:47. Single crystals formed after some days by solvent evaporation at room temperature and were analyzed by SC-XRD (single-crystal X-ray diffraction).

SS $PIR_xS\text{-}OXI_{1-x}$. The powder obtained from the mechanical grinding by ball milling of the PIR_x/S-OXI_{1-x} mixture with x = 0.5 was dissolved in ≈2 mL of water in a vial. A single crystal formed after some days by solvent evaporation at room temperature and was analyzed by SC-XRD.

SS $PIR_x\cdot R/S\text{-}OXI_{1-x}\cdot MgCl_2\cdot 5H_2O$. 100 mg of the mixture of PIR, RS-OXI, and $MgCl_2$ was prepared in the desired stoichiometric ratios (1:1:2 and 1:2:3) and dissolved in ≈2 mL of water in a vial. Single crystals formed after some days by slow solvent evaporation at room temperature and were analyzed by SC-XRD.

SS $PIR_x\cdot RS\text{-}OXI_{1-x}\cdot GA$. 100 mg of the mixture of PIR, RS-OXI, and GA was prepared in the desired stoichiometric ratios (0.5:0.5:1, 0.7:0.3:1, and 0.3:0.7:1) and dissolved in ≈2 mL of methanol in a vial. Single crystals formed after some days by solvent evaporation at room temperature and were analyzed by SC-XRD.

SS $PIR_x\cdot S\text{-}OXI_{1-x}\cdot GA$. Excessive amounts of PIR, S-OXI, and GA were slurried in methanol overnight to obtain saturated solutions. After this, a volume ratio of x:1−x:1 (PIR: S-OXI: GA, x ranging from 0 to 1) was added to a vial. The vials were left to evaporate slowly. See Supporting Information for the details.

Growth of Single Crystals from the Melt. 100 mg of the mixture of PIR and RS-OXI was prepared in the desired stoichiometric ratios (30:70, 50:50, 60:40, and 70:30). The powders were weighed and mixed in vials with a spatula. The vials were placed in a Thermo Scientific Vacutherm oven set at 160 °C for 1 h; a further 4 h were allowed for cooling to room temperature. After cooling, single crystals were collected and analyzed by SC-XRD, and the

Table 1. Crystal Data and Details of Measurement for SS 1 and SS 2 of $PIR_xRS\text{-}OXI_{1-x}$

	SS 1 $PIR_{0.22}RS\text{-}OXI_{0.78}$	*SS 1 $PIR_{0.44}RS\text{-}OXI_{0.56}$*	*SS 1 $PIR_{0.52}RS\text{-}OXI_{0.48}$*	*SS 1 $PIR_{0.62}RS\text{-}OXI_{0.38}$*	*SS 2 $PIR_{0.74}RS\text{-}OXI_{0.26}$*
Crystallization method	Solution crystallization water	Solution crystallization methanol	Melt crystallization	Melt crystallization	Melt crystallization
Reagent ratio PIR:RS-OXI	30:70	53:47	50:50	60:40	70:30
−OH occupancy	0.778(10)	0.56	0.478(7)	0.383(6)	0.262(19)
Formula	$C_6H_{10}N_2O_{2.78}$	$C_6H_{10}N_2O_{2.56}$	$C_6H_{10}N_2O_{2.48}$	$C_6H_{10}N_2O_{2.38}$	$C_6H_{10}N_2O_{2.26}$
Mw, g mol^{-1}	154.60	151.10	149.80	148.36	146.36
T/K	298.00	150	298.00	298.00	298.00
Crystal system	Orthorhombic	Orthorhombic	Orthorhombic	Orthorhombic	Monoclinic
Space group	$Pca2_1$	$Pca2_1$	$Pca2_1$	$Pca2_1$	$P2_1/n$
a/Å	8.8016(3)	8.6640(7)	8.7315(2)	8.7019(4)	6.7672(7)
b/Å	7.1359(2)	7.0865(6)	7.0992(2)	7.0912(4)	13.2640(14)
c/Å	11.4339(4)	11.3987(11)	11.6326(3)	11.6661(6)	8.2960(9)
α/°	90	90	90	90	90
β/°	90	90	90	90	100.159(7)
γ/°	90	90	90	90	90
V/Å^3	718.13(4)	699.86(11)	721.07(3)	719.88(6)	732.98(14)
Z, Z'	4, 1	4, 1	4, 1	4, 1	4, 1
ρ/g cm^{-3}	1.430	1.434	1.380	1.369	1.326
μ/mm^{-1}	0.967	0.113	0.913	0.899	0.862
Measd reflns	6522	5489	6587	6671	17158
Indep reflns	1298	1491	1300	1301	1304
Reflns with $I > 2\sigma(I)$	1281	1389	1284	1272	440
R_{int}	0.0430	0.0622	0.0312	0.0350	0.1358
R [$F^2 > 2\sigma(F^2)$]	0.0376	0.0401	0.0310	0.0313	0.0807
wR_2 (F^2)	0.0989	0.0922	0.0889	0.0854	0.2995

https://doi.org/10.1021/acs.cgd.5c00735
Cryst. Growth Des. 2025, 25, 6754−6763

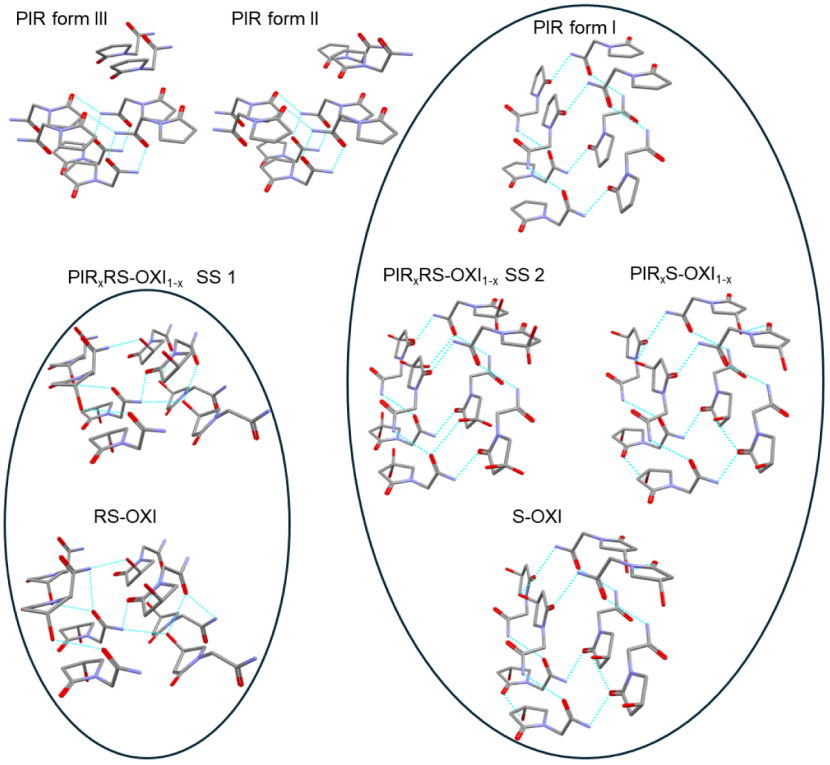

Figure 1. Representation of the crystal packing for PIR forms I, II, and III (CSD refcode BISMEV03, BISMEV, and BISMEV01, respectively), RS-OXI (CSD refcode DIRCAI), S-OXI (CSD refcode NUNBIK), and for PIR$_x$RS-OXI$_{1-x}$ SS 1, SS 2, and SS PIR$_x$S-OXI$_{1-x}$. In the cyrcles the set of isostructural forms; H atoms have been omitted for clarity.

remaining product was ground and analyzed by PXRD. See Supporting Information for details.

Powder X-ray Diffraction (PXRD). All diffraction patterns were recorded on a PANalytical EMPYREAN diffractometer system using Bragg–Brentano geometry and an incident beam of Cu Kα1,2 radiation (λ = 1.5418 Å) in the 2θ range between 3° and 40° (step size: 0.013°; time/step: 30 s; Soller slit: 0.04 rad; divergence slit: 1/8; antiscatter slit: 1/4; 45 mA × 40 kV). Room temperature scans were performed on a spinning silicon zero-background sample holder.

Thermal Analyses. Differential scanning calorimetry (DSC) measurements were performed on a TA DSC Q-2000 under a nitrogen stream (50 mL/min) using pierced pans and 4–6 mg of ground powder, between room temperature and 200 °C, at a 5 °C/min heating rate. Thermogravimetric measurements (TGA) were performed on a TA TGA Q-50 under a nitrogen stream (40 mL/min for the furnace and 60 mL/min for the balance) using 4–6 mg of ground powder, between room temperature and 300 °C, at a 5 °C/min heating rate.

Single-Crystal X-ray Diffraction. Single-crystal X-ray diffraction data were collected on a Bruker D8 Quest diffractometer equipped with either Cu Kα (λ = 1.54178 Å) radiation or Mo Kα (λ = 0.71073 Å) radiation and a Photon 100 detector. The data were integrated with Apex 4. The structures were solved by intrinsic phasing methods and refined by least-squares methods against F^2 using SHELXT[36] and SHELXL[37] through the OLEX2 interface.[38] Non-hydrogen atoms were refined anisotropically, while hydrogen atoms were placed in calculated positions. The software Mercury[39] was used for graphical representations. Single-crystal X-ray diffraction data were also obtained using a MAR345 image plate detector and Mo Kα radiation (λ = 0.71073 Å) produced by an Incoatec IμS microfocus source. All acquired data were integrated and reduced using CrysAlis^{PRO}. These structures were solved using the dual-space algorithm in SHELXT and further refined against F^2 using SHELXL. The relative occupancy of the H/OH groups on the C4 position was determined by introducing additional free variables: one for PIR$_x$RS-OXI$_{1-x}$ SS 1, PIR$_x$S-OXI$_{1-x}$, and PIR$_x$·R/S-OXI$_{1-x}$·$MgCl_2$·$5H_2O$; two for PIR$_x$RS-OXI$_{1-x}$ SS 2; and three for PIR$_x$·RS-OXI$_{1-x}$·GA. The O atoms were refined anisotropically, and their occupancy was used to determine the chemical composition of the solid solutions. Unit cell parameters for all compounds discussed herein are reported in Tables 1 and S3–S6.

DVS. Water vapor sorption isotherm measurements were performed using an Advantage dynamic vapor sorption (DVS) instrument manufactured by Surface Measurement Systems. The instrument gravimetrically measures water vapor uptake using air as a carrier gas. Digital mass flow controllers regulate the flows of dry and saturated gases. Relative humidity is generated by precisely mixing dry and saturated gas flows in desired flow ratios, which produce the expected relative humidity. Pure water was used to generate water vapor for these measurements, and the temperature was maintained at 298 K by enclosing the system in a temperature-controlled incubator. The mass of the sample was determined with a high-resolution microbalance with a precision of 0.01 μg. The microbalance has a symmetric configuration, with two branches of the balance being exposed to the same gas and kept at the same temperature, which allows for the negation of buoyancy and drag effects. The instrument allows the measurement of 2 samples in parallel. 200 sccm min^{-1} was used for the measurements at 298 K. The flow is split between two samples. Water sorption isotherm measurements were performed across the range of 0–95% RH. For each isotherm point, dm/dt <0.01%/min was used as the criterion for reaching equilibrium.

Construction of Phase Diagrams. PIR, RS-OXI, and GA were ground together in a ratio of x:1-x:1, with x ranging from 0 to 1. After that, a portion of the mixture was added to a 5 mL vial, and the solid was left to slurry in a small amount of MeOH, ACN, and MeOH/H_2O (v/v = 80/20) for 6 h. Subsequently, solvent was added to the vial every 30 min, until the suspension became clear. The total amount of solvent added allowed us to plot the solubility curve on the phase diagram.

https://doi.org/10.1021/acs.cgd.5c00735
Cryst. Growth Des. 2025, 25, 6754–6763

RESULTS AND DISCUSSION

Piracetam (PIR) and Oxiracetam (OXI) are common prescription drugs used for the treatment of central nervous system disorders, such as cognitive/memory impairment, dysfunctions, epilepsy, and neurodegenerative diseases.[40,41]

OXI is structurally related to PIR, with the proton in position 4 replaced by a hydroxyl group (Chart 1), which confers chirality to the molecule. OXI is used as a racemic mixture, of which the *S* enantiomer is the active ingredient,[42] and provides a more stimulating effect than PIR, with additional benefits on cognition, concentration, and memory.[43]

Crystal forms of PIR and OXI have been extensively screened: polymorphs, molecular, and ionic cocrystals are reported,[31,33,44−48] but no SSs. Indeed, the chemical differences of the two drugs translate into crystallographic differences, whereby the amide group sustains the typical H-bond dimer in the most stable polymorphs of PIR (CSD refcode BISMEV[49] and BISMEV01,[49] respectively forms II and III), but it is involved in a 3D H-bond network together with the hydroxyl group in OXI (Figure 1). PIR shows a different H-bond network above 120 °C, in the metastable form I (CSD refcode BISMEV03;[50] Figure 1), which rapidly reverts to form II at ambient temperature.[51] As a result, the only structure known for the racemate is different from any of the five forms reported for PIR (Table S1). However, the enantiopure S-OXI (CSD refcode NUNBIK)[31] is isostructural with PIR I, apart from the additional H-bond and lower symmetry (space group $P2_1$ vs $P2_1/n$; Figure 1).

Molecular Solid Solutions. *SS PIR$_x$RS-OXI$_{1-x}$.* Single crystals of PIR$_x$RS-OXI$_{1-x}$ (SS 1) were obtained by the slow evaporation of a water solution of PIR and RS-OXI in a 30:70 ratio. SS 1 crystallizes in the orthorhombic crystal system, space group $Pca2_1$ (Table 1) isomorphous to RS-OXI (CSD refcode DIRCAI;[52] Figure 1). Occupancy refinement of the −OH group for the selected single crystal showed a PIR:RS-OXI ratio of 22:78. A single crystal of SS 1 with a higher amount of PIR (x = 0.44) was obtained by crystallization from methanol (Table 1) confirming that PIR molecules can enter the dense hydrogen bond network that sustains the columnar structure of RS-OXI (Figure 2a). In either case, the bulk products were not pure, and traces of PIR form II were detected by PXRD (Figure S2), which would represent a significant issue in the commercialization of any drug. Liquid-assisted grinding of different ratios of PIR and RS-OXI with EtOH by ball milling resulted in physical mixtures of RS-OXI and PIR form III, except for the 15:85 PIR:RS-OXI ratio, where peaks of PIR disappear, suggesting the formation of SS 1 (Figure S3). Notably, manual grinding of the same stoichiometry resulted in a physical mixture (Figure S3), highlighting the importance of the synthetic methods for the preparation of solid solutions.[26,27,53] In fact, a pure and homogeneous product was obtained by cooling the melt solution.[16,54−56]

RS-OXI melts at 168 °C, while PIR, after transforming into form I at ≈120 °C, melts at 152 °C, and both decompose above ≈165 °C (Figures S15 and S16). Slow cooling of the melt solution of PIR and RS-OXI in an oven from 160 °C to RT produced a hard aggregate of single crystals. SC-XRD analysis confirms the formation of SS 1 PIR$_x$RS-OXI$_{1-x}$ for $x \leq 0.6$ (Table 1 and Figure S4). Comparison of the unit cells of the crystals measured at RT shows a small contraction of the *a*-parameter, which correlates with the increase of PIR (refined occupancy) in the crystal structure (Figure 3). Such behavior is justified by the reduced steric hindrance of the proton and causes a linear elongation of the *c*-axis (Figures 2a and 3).

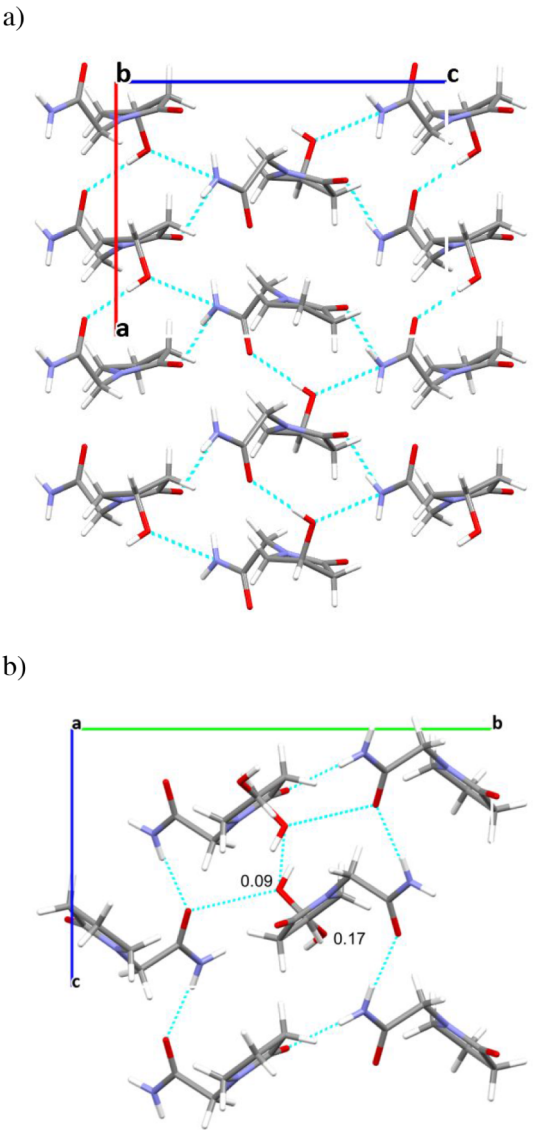

Figure 2. Representation for: (a) the crystal packing of SS 1 (view along the crystallographic *b*-axis) and (b) the crystal packing of SS 2 (view along the *a*-axis); H-bonds are shown as cyan dashed lines.

PXRD analysis of the bulk product confirmed the formation of SS 1 for $x \leq 0.6$ (x = 0.3, 0.5, and 0.6) without traces of other phases (Figure 4). In the diffractograms, it is possible to notice a constant shift toward lower degrees (higher *d*-spacing) for the (002) peak, and toward higher degrees for the (201) peak, as the percentage of PIR in the mixture increases (Figure 4), in agreement with the elongation of the *c*-axis and shortening of the *a*-axis. However, a different phase was observed for $x \geq 0.7$, as determined by SC-XRD analysis. PIR$_{0.74}$RS-OXI$_{0.26}$ crystallizes in the monoclinic crystal system, space group $P2_1/n$ (SS 2), and it is isostructural to high temperature PIR form I (Tables 1 and S1 and Figures S5 and 1). Analysis of the precession images confirms that the solid solution includes both enantiomers in the centrosymmetric space group rather than a conglomerate of the two chiral $P2_1$ structures of enantiopure OXI. As a result, the −OH group is disordered over two positions; the one with the lower

https://doi.org/10.1021/acs.cgd.5c00735
Cryst. Growth Des. 2025, 25, 6754−6763

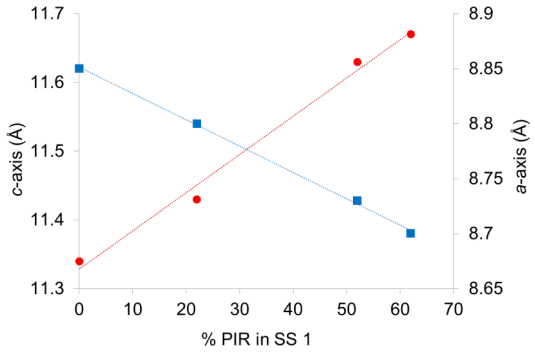

Figure 3. Linear dependence between the dimension of the *c*-axis (red circle markers) and *a*-axis (blue square markers) and the percentage of PIR present in SS 1 (data collected at 298 K; for pure RS-OXI, the cell parameters of the structure deposited in the CSD, refcode DIRCAI,[52] were used).

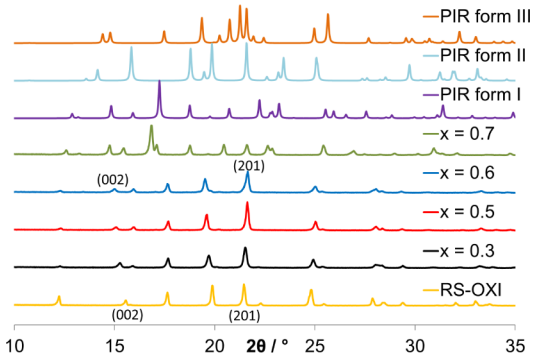

Figure 4. Comparison of the experimental PXRD patterns for the product of the crystallization from the melt of PIR_x/RS-OXI_{1-x} mixtures with x = 0.3, 0.5, 0.6, and 0.7. At the bottom, the experimental pattern of RS-OXI is shown, and at the top, the calculated pattern for PIR forms I, II, and III (CSD refcode BISMEV03, BISMEV, and BISMEV01, respectively).

occupancy is the position that leads to the formation of H-bonds absent in the parental PIR form I and to a greater steric hindrance between adjacent molecules (Figure 2b).

Differential scanning calorimetry (DSC) shows the SSs to have a lower melting point compared with both PIR and RS-OXI (Figure S17). SS 1 shows the MP onset at 136 °C for x = 0.3, which decreases to 125 °C at x = 0.5. SS 2 (x = 0.7) melts at 132 °C. The eutectic behavior, as well as the broad endothermic peaks, is consistent with two-sided solid solutions characterized by crystals with a wide compositional spread.

Ultimately, PIR and RS-OXI are mutually soluble at all compositions in the solid state although the crystalline structure of the SS changes at around 60−70% PIR, which is expected when the pure compounds do not share common structures.[29] The observed stoichiometric limits are indicative and probably sensitive to the experimental conditions. In fact, crystallization from the melt of PIR_x/RS-OXI_{1-x} mixtures with x = 0.5, obtained with a more rapid cooling rate, resulted in a mixture of SS 1 and SS 2 (Figure S9).

Most importantly, in SS2, the high-temperature structure of PIR remains stable for several months, whereas form I converts to form II within hours for pure PIR.[51] In our case, traces of SS 1 only appear after 1 year (Figure S6).

SS PIR_xS-OXI_{1-x}. When enantiopure S-OXI was ground by ball milling together with PIR in the presence of a few drops of EtOH, a phase isomorphous to that of S-OXI was observed in the PXRD patterns. The peaks of this phase shift regularly with the stoichiometry of the reagents (Figure 5). As the amount of

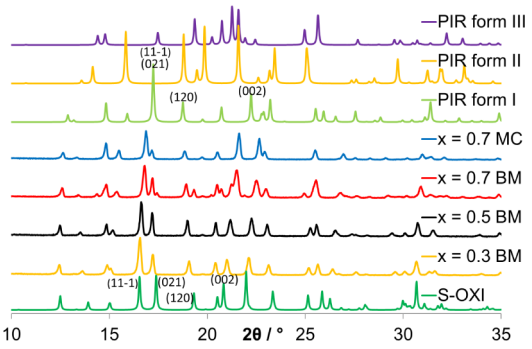

Figure 5. Comparison of the experimental PXRD patterns for the product of mechanical grinding by ball milling of PIR_x/S-OXI_{1-x} mixtures with x = 0.3, 0.5, and 0.7; the product of crystallization from the melt (MC) of the PIR_x/S-OXI_{1-x} mixture with x = 0.7; the calculated pattern for S-OXI (CSD refcode NUNBIK); and, at the top, the calculated pattern for PIR forms I, II, and III (CSD refcodes BISMEV03, BISMEV, and BISMEV01, respectively).

PIR in the mixture PIR_xS-OXI_{1-x} (x = 0.3, 0.5, and 0.7) increases, the peaks shift toward the calculated pattern of PIR form I, suggesting a continuous variation of the cell metrics (see Table S1 for parent compounds), and thus the formation of SS PIR_xS-OXI_{1-x}. For example, peak (002) undergoes a strong shift toward larger angles, indicating a shortening of the *c*-axis.

Mechanical grinding did not provide a pure phase over the entire composition range; in fact, for x = 0.7, in addition to the SS phase, traces of PIR form III are also visible in the diffractogram. Once again, crystallization from the melt provided a pure SS (Figure 5). Single crystals were obtained by recrystallization from a water solution of the $PIR_{0.5}S$-$OXI_{0.5}$ powder obtained by mechanical grinding. SC-XRD analysis confirmed the crystallization of SS PIR_xS-OXI_{1-x} (x = 0.48) in $P2_1$ (Figure S7 and Table S5), isostructural to S-OXI and PIR form I (Figure 1); the unit cell parameters are intermediate between those of the two forms. Consequently, SS PIR_xS-OXI_{1-x} is also isostructural to SS 2 (Figure 1); however, whereas SS 2 showed traces of SS 1 after about a year, the SS containing enantiopure OXI remains stable for over 1 year (Figure S8).

CoCrystalline Solid Solutions. In principle, the reduced kinetics enable the commercialization of metastable, more soluble phases. However, the delicate interplay between the composition and synthetic conditions represents a problem. With this in mind, cocrystalline solid solutions (CCSS) of PIR and RS-OXI were screened to identify those that could afford a single phase over the whole compositional range. Two CCSSs were successfully obtained, employing either $MgCl_2$ or gallic acid (GA) as coformers.

SS PIR_x·R-OXI_{1-x}·$MgCl_2$·5H_2O and SS PIR_x·S-OXI_{1-x}·$MgCl_2$·5H_2O. Manual grinding of RS-OXI with $MgCl_2$ results in the formation of the ionic cocrystal conglomerate S-OXI·$MgCl_2$·5H_2O and R-OXI·$MgCl_2$·5H_2O, as reported by Shemchuk et al. (CSD refcode NUMZUT for the enantiopure S-OXI·$MgCl_2$·5H_2O).[31] A similar phase was also observed when liquid-assisted grinding was performed by adding different amounts of PIR and RS-OXI to $MgCl_2$. A few peaks of this phase undergo a regular shift depending on the PIR:RS-OXI

https://doi.org/10.1021/acs.cgd.5c00735
Cryst. Growth Des. 2025, 25, 6754−6763

ratio (Figures S10 and 6), indicating the formation of a SS. Unfortunately, when the ratio of PIR:RS-OXI exceeds 2:1,

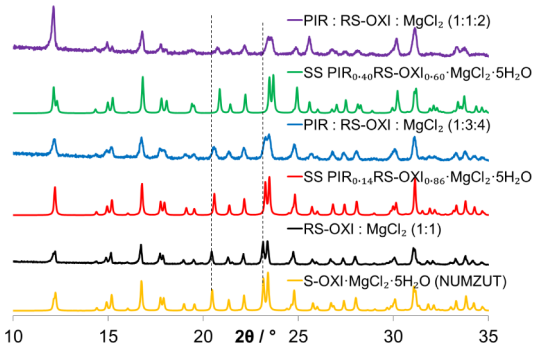

Figure 6. Comparison of experimental PXRD patterns for the product of manual grinding of PIR/RS-OXI/$MgCl_2$ mixtures with different stoichiometric ratios and the calculated patterns for SS $PIR_xRS\text{-}OXI_{1-x}\cdot MgCl_2\cdot 5H_2O$. From bottom to top: the calculated pattern of S-OXI·$MgCl_2$·$5H_2O$ (CSD refcode NUMZUT), the experimental pattern for the product of the manual grinding of the RS-OXI/$MgCl_2$ mixture (1:1), the calculated pattern of the SS $PIR_{0.14}RS\text{-}OXI_{0.86}\cdot MgCl_2\cdot 5H_2O$, the experimental pattern for the product of manual grinding of the PIR/RS-OXI/$MgCl_2$ mixture (1:3:4), the calculated pattern of the SS $PIR_{0.40}RS\text{-}OXI_{0.60}\cdot MgCl_2\cdot 5H_2O$, and the experimental pattern for the product of manual grinding of PIR/RS-OXI/$MgCl_2$ mixture (1:1:2).

crystallinity decreases, and the powder becomes increasingly hygroscopic until a deliquescent product is obtained for pure PIR and $MgCl_2$ in a 1:1 ratio. Different phases were obtained from manual grinding and ball milling of the PIR/$MgCl_2$ mixture in a 2:1 ratio (Figure S10), but these powders also became deliquescent within minutes. Single crystals were grown by slow evaporation of water solutions of PIR/RS-OXI/$MgCl_2$ mixtures in different stoichiometric ratios (1:1:2 and 1:2:3) and analyzed by means of SC-XRD. Structure determination and occupancy refinement showed a monoclinic $P2_1$ phase, isostructural to *S*-OXI·$MgCl_2$·$5H_2O$ (CSD refcode NUMZUT),[31] with a relative OXI amount of 60% for the 1:1 ratio crystallization (Figure 6 and Tables S2 and S3), confirming the formation of the ionic cocrystal solid solution (ICCSS)[57] as a conglomerate of $PIR_x\cdot R\text{-}OXI_{1-x}\cdot MgCl_2\cdot 5H_2O$ and $PIR_x\cdot S\text{-}OXI_{1-x}\cdot MgCl_2\cdot 5H_2O$ ($PIR_x\cdot R/S\text{-}OXI_{1-x}\cdot MgCl_2\cdot 5H_2O$). Notably, the pure ionic cocrystals and their solid solutions are stable if dried and stored in an Eppendorf vial for over 1 year (Figure S14).

The Mg^{2+} cations are octahedrally coordinated to four water molecules and two OXI/PIR molecules in the *cis* position. Drug molecules bridge two Mg^{2+} through the pyrrolidone carbonyl and the amide carbonyl, forming infinite chains along the crystallographic *b*-axis.[31] The chloride anions are not coordinated but form H-bond to water, amides, and the −OH group of the OXI (Figure 7). It is noteworthy that, despite the large amount of PIR present in the solid, spontaneous chiral resolution of RS-OXI with formation of conglomerate crystals is still obtained.

Thermogravimetric analysis of the SS powders showed a gradual initial weight loss below 100 °C, which becomes more pronounced with an increasing amount of piracetam in SS; this is probably due to the increase in surface water adsorbed on the powders (Figure S18). DVS isotherm analysis (Figures 8 and S19−S21) confirmed that the SS becomes more

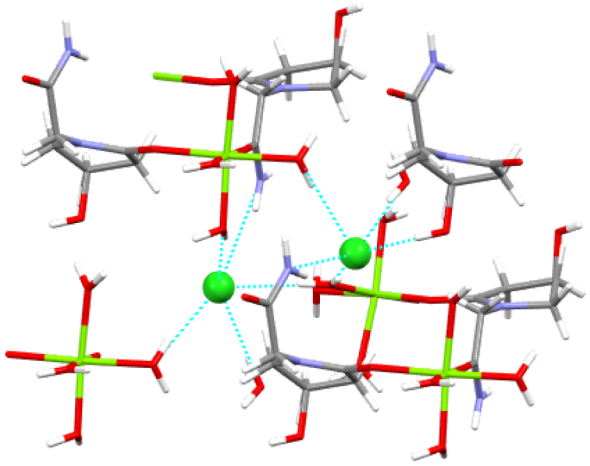

Figure 7. Crystal packing of SS $PIR_x\cdot R/S\text{-}OXI_{1-x}\cdot MgCl_2\cdot 5H_2O$, showing the H-bonds (cyan dashed lines) with the chloride anions (green spheres).

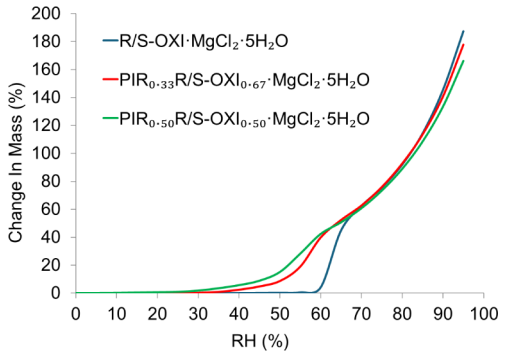

Figure 8. DVS isotherm analysis for the cocrystal R/S-OXI·$MgCl_2$·$5H_2O$ (blue line), the solid solutions $PIR_{0.33}\cdot R/S\text{-}OXI_{0.67}\cdot MgCl_2\cdot 5H_2O$ (red line), and $PIR_{0.5}\cdot R/S\text{-}OXI_{0.5}\cdot MgCl_2\cdot 5H_2O$ (green line).

hygroscopic as the PIR:RS-OXI ratio increases: the R/S-OXI·$MgCl_2$·$5H_2O$ cocrystal takes up a significant amount of water vapor when the RH exceeds 60%, whereas for the SS, the critical relative humidity decreases constantly, until it reaches approximately 35% for the solid solution $PIR_{0.5}\cdot R/S\text{-}OXI_{0.5}\cdot MgCl_2\cdot 5H_2O$. We speculate that the increased hygroscopicity is the consequence of additional H-bond capability for the chlorine in the absence of the hydroxyl group of OXI.[58,59] If stored in a closed vial, the ICCSS $PIR_{0.5}\cdot R/S\text{-}OXI_{0.5}\cdot MgCl_2\cdot 5H_2O$ is stable for more than 1 year (Figure S14). In any case, such hygroscopicity would be undesirable for commercial solid forms of drugs.

SS PIR_x·RS-OXI_{1-x}·GA. Given the high hygroscopicity of the ICCSS, a molecular cocrystal SS was sought with gallic acid (GA). GA has been shown to improve the hygroscopic stability of S-OXI,[33] and notably, the cocrystal (S-OXI·GA, CSD refcode: ZEBXEL, $P2_1$)[33] is isostructural to that of PIR (PIR·GA, CSD refcode AKISEU, $P2_1/c$)[32] and RS-OXI (RS-OXI·GA, CSD refcode: ZEBXIP, $P2_1/c$; Table S2).[33] In fact, the molecular arrangement in the three cocrystals is the same, and the H-bonds of the hydroxyl substituent do not seem essential to sustain these crystal structures (Figure 9).

Slow solvent evaporation from a methanol solution of GA with PIR and RS-OXI in different ratios afforded single crystals suitable for SC-XRD analysis. Structure determination and −OH occupancy refinement revealed a SS $PIR_x\cdot RS\text{-}OXI_{1-x}\cdot$

https://doi.org/10.1021/acs.cgd.5c00735
Cryst. Growth Des. 2025, 25, 6754−6763

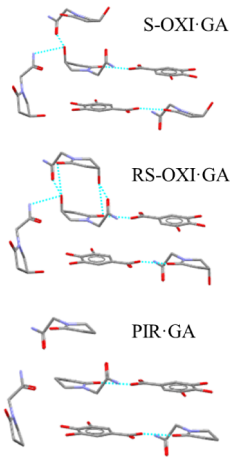

Figure 9. Comparison of the crystal packing for S-OXI·GA (CSD refcode ZEBXEL), RS-OXI·GA (CSD refcode ZEBXIP), and PIR·GA (CSD refcode AKISEU); H-bonds are shown as blue dashed lines, and H atoms are omitted for clarity.

GA, which crystallizes in a monoclinic $P2_1/c$ space group (Table S4) isostructural to the respective cocrystals of GA with PIR (AKISEU) and RS-OXI (ZEBXIP, Table S2). Depending on the ratio used in the methanol solution, different percentages of PIR and OXI were found in the single crystals (Table S4). Since crystallization from solution usually does not yield crystals with a homogeneous composition,[16,22] mechanical grinding by ball milling of PIR/RS-OXI/GA mixtures was performed in the presence of a few drops of ethyl acetate. The product obtained is a dry, non-hygroscopic powder, and the PXRD patterns show a pure phase isomorphous to RS-OXI·GA and PIR·GA, as expected, with a smooth peak shift dependent on the PIR:RS-OXI ratio, confirming the formation of a homogeneous solid solution over the whole composition (Figures 10, S11, and S12). Moreover, this SS was stable for over 6 months (Figure S13).

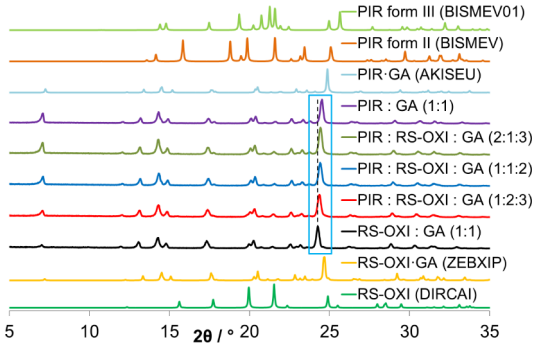

Figure 10. Comparison of the experimental PXRD patterns for the product of mechanical grinding of PIR/RS-OXI/GA mixtures with different stoichiometric ratios. From bottom to top: calculated pattern of RS-OXI (CSD refcode DIRCAI), calculated for RS-OXI·GA (CSD refcode ZEBXIP), experimental pattern for the product of mechanical grinding of RS-OXI/GA mixture (1:1), the experimental patterns for the product of mechanical grinding of PIR/RS-OXI/GA mixtures with 1:2:3, 1:1:2, and 2:1:3 ratios, experimental pattern for the product of mechanical grinding of PIR/GA mixture (1:1), calculated for PIR·GA (CSD refcode AKISEU), and the calculated pattern for PIR forms II and III (CSD refcode BISMEV and BISMEV01, respectively); AKISEU and ZEBXIP are collected at 100 K.

SS PIR_x·S-OXI_{1-x}·GA. Crystallizations by slow solvent evaporation from saturated methanol solutions of PIR and enantiopure S-OXI with GA led to the formation of single crystals. X-ray diffraction analysis revealed a monoclinic $P2_1$ structure, identical to that of S-OXI·GA and PIR·GA (Tables S2 and S6). Unit cell parameters change linearly with the composition (Figure 11). Once again, different amounts of PIR

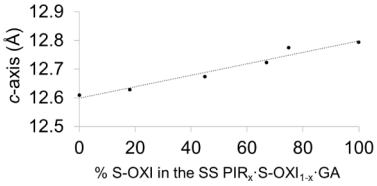

Figure 11. Linear dependence between the *c*-axis dimension and the percentage of S-OXI present in the solid solution PIR_x·S-OXI_{1-x}·GA.

and S-OXI were found in the crystals depending on the stoichiometric ratio used for the crystallization, confirming a SS PIR_x·S-OXI_{1-x}·GA over the entire range $0 < x < 1$.

Phase Diagram for SS PIR_x·RS-OXI_{1-x}·GA. The construction of ternary phase diagrams can guide and optimize the crystallization process. As shown in Figure 12 (Figure S22 for the full diagrams), three ternary phase diagrams were constructed in MeOH, ACN, and MeOH/H_2O (v/v) = 80/20 at 30 °C, where the red line with symbols represents the saturated-liquid line. As the amount of PIR incorporated into the crystal lattice of RS-OXI·GA increases, the solubility of SS PIR_x·RS-OXI_{1-x}·GA increases in all three solvents. This solubility behavior can be helpful in the design of a crystallization process. Based on the ternary diagrams, the crystallization conditions can be optimized by adjusting the amounts of PIR, RS-OXI, and solvent. The phase diagrams also confirm that an SS is obtained over the full stoichiometric range.

CONCLUSION

Despite the different chemical structures and H-bond capabilities, which are reflected in their crystal form landscape, PIR and RS-OXI crystallize into multiple molecular solid solutions, including SSs, CCSSs, and ICCSSs. Crystallization from the melt proved the mutual solubility of the molecules (virtually) over the entire compositional range, although in different crystal forms depending on the ratio of the two drugs. When the same experiment is repeated between PIR and the enantiopure S-OXI, a single SS is obtained, also mechanochemically, stabilizing a metastable crystal form otherwise accessible only at high temperature.

The use of coformers simplifies the synthetic requirements for the PIR/OXI solid-state solubility in the ionic cocrystal solid solution with $MgCl_2$, although the high hygroscopicity prevents any practical application of the product, especially at high PIR content. In contrast, the hygroscopicity is reduced in the cocrystalline solid solution with the organic cofomer GA. This SS is obtained over the whole composition from solution crystallization or mechanochemical methods, and it is stable over time.

It is known that the presence or absence of a hydroxyl group in APIs can dramatically affect physicochemical properties and biological activity within a family of drug molecules.[60−63] This work opens to their solid solutions confirming solid-state solubility between molecules with different H-bond capabilities

https://doi.org/10.1021/acs.cgd.5c00735
Cryst. Growth Des. 2025, 25, 6754−6763

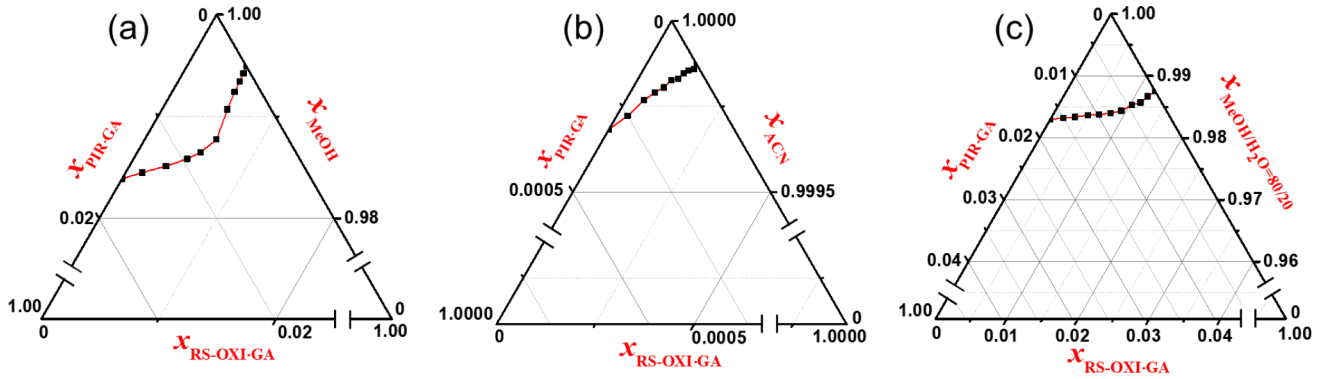

Figure 12. Ternary phase diagrams of SS PIR_x·RS-OXI_{1-x}·GA constructed in three solvents at 30 °C: (a)MeOH; (b)ACN; (c)MeOH/H_2O (v/v) = 80/20.

can be realized.[30] More importantly, this work highlights that (i) the solid-state landscape of solid solutions can be as rich as that of pure substances; (ii) multiple synthetic and crystal design strategies should be employed to explore it; and (iii) significant variations in structural and physicochemical properties are expected that allows the precise control of drug stoichiometry in a single crystalline phase for targeted therapies for better patient compliance and (possibly) pharmacokinetic performances.

■ ASSOCIATED CONTENT

Supporting Information

The Supporting Information is available free of charge at https://pubs.acs.org/doi/10.1021/acs.cgd.5c00735.

PXRD, crystallographic data, thermograms, and DVS isotherm analyses (PDF)

Accession Codes

Deposition Numbers 2452743−2452759 contain the supplementary crystallographic data for this paper. These data can be obtained free of charge via the joint Cambridge Crystallographic Data Centre (CCDC) and Fachinformationszentrum Karlsruhe Access Structures service.

■ AUTHOR INFORMATION

Corresponding Authors

Tom Leyssens − *Institute of Condensed Matter and Nanosciences, Université catholique de Louvain, Louvain-La-Neuve 1348, Belgium;* orcid.org/0000-0001-7916-1373; Email: tom.leyssens@uclouvain.be

Matteo Lusi − *Department of Chemical Sciences & Bernal Institute, University of Limerick, Limerick V94 T9PX, Ireland;* orcid.org/0000-0002-9067-7802; Email: matteo.lusi@ul.ie

Authors

Enrico Spoletti − *Department of Chemical Sciences & Bernal Institute, University of Limerick, Limerick V94 T9PX, Ireland*

Ting Wen − *Institute of Condensed Matter and Nanosciences, Université catholique de Louvain, Louvain-La-Neuve 1348, Belgium*

Fucheng Leng − *Institute of Condensed Matter and Nanosciences, Université catholique de Louvain, Louvain-La-Neuve 1348, Belgium*

Nathan Boukioud − *Department of Chemical Sciences & Bernal Institute, University of Limerick, Limerick V94 T9PX, Ireland*

Jason Carty Lacey − *Department of Chemical Sciences & Bernal Institute, University of Limerick, Limerick V94 T9PX, Ireland*

Shaza Darwish − *Department of Chemical Sciences & Bernal Institute, University of Limerick, Limerick V94 T9PX, Ireland;* orcid.org/0000-0001-9397-6886

Oleksii Shemchuk − *Institute of Condensed Matter and Nanosciences, Université catholique de Louvain, Louvain-La-Neuve 1348, Belgium;* orcid.org/0000-0003-3003-3922

Koen Robeyns − *Institute of Condensed Matter and Nanosciences, Université catholique de Louvain, Louvain-La-Neuve 1348, Belgium;* orcid.org/0000-0002-4763-4217

Complete contact information is available at: https://pubs.acs.org/10.1021/acs.cgd.5c00735

Notes

The authors declare no competing financial interest.

■ ACKNOWLEDGMENTS

E.S. and M.L. thank the Bernal Institute, Boston Scientific, the Department of Chemical Sciences, and the University of Limerick Foundation for funding support enabling this research through the mULtiply program.

■ REFERENCES

(1) Thakuria, R.; Delori, A.; Jones, W.; Lipert, M. P.; Roy, L.; Rodríguez-Hornedo, N. Pharmaceutical cocrystals and poorly soluble drugs. *Int. J. Pharm.* **2013**, *453* (1), 101−125.

(2) Steed, J. W. The role of co-crystals in pharmaceutical design. *Trends Pharmacol. Sci.* **2013**, *34* (3), 185−193.

(3) Braga, D.; Grepioni, F.; Shemchuk, O. Organic−inorganic ionic co-crystals: a new class of multipurpose compounds. *CrystEngcomm* **2018**, *20* (16), 2212−2220.

(4) Grepioni, F.; Braga, D.; Chelazzi, L.; Shemchuk, O.; Maffei, P.; Sforzini, A.; Viscomi, G. Improving solubility and storage stability of rifaximin via solid-state solvation with Transcutol®. *CrystEngcomm* **2019**, *21* (35), 5278−5283.

(5) Wang, J.; Dai, X.-L.; Lu, T.-B.; Chen, J.-M. Temozolomide−hesperetin drug−drug cocrystal with optimized performance in stability, dissolution, and tabletability. *Cryst. Growth Des.* **2021**, *21* (2), 838−846.

(6) Thipparaboina, R.; Kumar, D.; Chavan, R. B.; Shastri, N. R. Multidrug co-crystals: towards the development of effective therapeutic hybrids. *Drug Discovery Today* **2016**, *21* (3), 481−490.

(7) Almansa, C.; Merce, R.; Tesson, N.; Farran, J.; Tomàs, J.; Plata-Salamán, C. R. Co-Crystal of Tramadol hydrochloride−Celecoxib (CTC): a novel API−API co-crystal for the treatment of pain. *Cryst. Growth Des.* **2017**, *17* (4), 1884−1892.

(8) Sica, D. A. Fixed-dose combination antihypertensive drugs: do they have a role in rational therapy? *Drugs* **1994**, *48*, 16−24.
(9) Bell, D. Combine and conquer: advantages and disadvantages of fixed-dose combination therapy. *Diabetes Obes. Metab.* **2013**, *15* (4), 291−300.
(10) Gascon, N.; Almansa, C.; Merlos, M.; Miguel Vela, J.; Encina, G.; Morte, A.; Smith, K.; Plata-Salamán, C. Co-crystal of tramadol-celecoxib: preclinical and clinical evaluation of a novel analgesic. *Expert Opin. Invest. Drugs* **2019**, *28* (5), 399−409.
(11) Fala, L. Entresto (Sacubitril/Valsartan): first-in-class angiotensin receptor neprilysin inhibitor FDA approved for patients with heart failure. *Am. Health Drug Benefits* **2015**, *8* (6), 330.
(12) Kavanagh, O. N. An analysis of multidrug multicomponent crystals as tools for drug development. *J. Controlled Release* **2024**, *369*, 1−11.
(13) Lusi, M. Engineering crystal properties through solid solutions. *Cryst. Growth Des.* **2018**, *18* (6), 3704−3712.
(14) Lusi, M. A rough guide to molecular solid solutions: design, synthesis and characterization of mixed crystals. *CrystEngcomm* **2018**, *20* (44), 7042−7052.
(15) Fonseca, J. D. C.; Tenorio Clavijo, J. C.; Alvarez, N.; Ellena, J.; Ayala, A. P. Novel solid solution of the antiretroviral drugs lamivudine and emtricitabine. *Cryst. Growth Des.* **2018**, *18* (6), 3441−3448.
(16) Spoletti, E.; Verma, V.; Cappuccino, C.; Lusi, M. Solid solution polymorphs afford two highly soluble co-drug forms of tolbutamide and chlorpropamide. *Chem. Commun.* **2023**, *59* (96), 14321−14324.
(17) Kitaigorodsky, A. I. *Mixed crystals*; Springer Science & Business Media, 2012.
(18) Case, D. H.; Srirambhatla, V. K.; Guo, R.; Watson, R. E.; Price, L. S.; Polyzois, H.; Cockcroft, J. K.; Florence, A. J.; Tocher, D. A.; Price, S. L. Successful computationally directed templating of metastable pharmaceutical polymorphs. *Cryst. Growth Des.* **2018**, *18* (9), 5322−5331.
(19) Chakraborty, S.; Joseph, S.; Desiraju, G. R. Probing the Crystal Structure Landscape by Doping: 4-Bromo, 4-Chloro, and 4-Methylcinnamic Acids. *Angew. Chem. Int. Ed.* **2018**, *57* (30), 9279−9283.
(20) Adams, C. J.; Haddow, M. F.; Lusi, M.; Orpen, A. G. Crystal engineering of lattice metrics of perhalometallate salts and MOFs. *Proc. Int. Acad. Sci.* **2010**, *107* (37), 16033−16038.
(21) Braun, D. E.; Kahlenberg, V.; Griesser, U. J. Experimental and computational hydrate screening: cytosine, 5-flucytosine, and their solid solution. *Cryst. Growth Des.* **2017**, *17* (8), 4347−4364.
(22) Schur, E.; Nauha, E.; Lusi, M.; Bernstein, J. Kitaigorodsky revisited: polymorphism and mixed crystals of acridine/phenazine. *Chem. Eur. J.* **2015**, *21* (4), 1735−1742.
(23) Cruz-Cabeza, A. J.; Lestari, M.; Lusi, M. Cocrystals Help Break the "Rules" of Isostructurality: Solid Solutions and Polymorphism in the Malic/Tartaric Acid System. *Cryst. Growth Des.* **2018**, *18* (2), 855−863.
(24) Lestari, M.; Lusi, M. A mixed molecular salt of lithium and sodium breaks the Hume-Rothery rules for solid solutions. *Chem. Commun.* **2019**, *55* (16), 2297−2300.
(25) Oliveira, M. A.; Peterson, M. L.; Klein, D. Continuously substituted solid solutions of organic co-crystals. *Cryst. Growth Des.* **2008**, *8* (12), 4487−4493.
(26) Lusi, M.; Vitorica-Yrezabal, I. J.; Zaworotko, M. J. Expanding the scope of molecular mixed crystals enabled by three component solid solutions. *Cryst. Growth Des.* **2015**, *15* (8), 4098−4103.
(27) Lusi, M.; Atwood, J. L.; MacGillivray, L. R.; Barbour, L. J. Isostructural coordination polymers: Epitaxis vs. solid solution. *CrystEngcomm* **2011**, *13* (13), 4311−4313.
(28) Lestari, M.; Lusi, M.; O'Leary, A.; O'Nolan, D.; Zaworotko, M. J. Hygroscopicity of lithium coordination polymers and their solid solutions. *CrystEngcomm* **2018**, *20* (39), 5940−5944.
(29) Hill, A.; Kras, W.; Theodosiou, F.; Wanat, M.; Lee, D.; Cruz-Cabeza, A. J. Polymorphic solid solutions in molecular crystals: Tips, tricks, and switches. *J. Am. Chem. Soc.* **2023**, *145* (37), 20562−20577.
(30) Verma, V.; Bordignon, S.; Chierotti, M. R.; Lestari, M.; Lyons, K.; Padrela, L.; Ryan, K. M.; Lusi, M. Cortisone and cortisol break hydrogen-bonding rules to make a drug−prodrug solid solution. *IUCrJ.* **2020**, *7* (6), 1124−1130.
(31) Shemchuk, O.; Song, L.; Tumanov, N.; Wouters, J.; Braga, D.; Grepioni, F.; Leyssens, T. Chiral resolution of RS-oxiracetam upon cocrystallization with pharmaceutically acceptable inorganic salts. *Cryst. Growth Des.* **2020**, *20* (4), 2602−2607.
(32) Thomas, L. H.; Wales, C.; Wilson, C. C. Selective preparation of elusive and alternative single component polymorphic solid forms through multi-component crystallisation routes. *Chem. Commun.* **2016**, *52* (46), 7372−7375.
(33) Wang, Z.-Z.; Chen, J.-M.; Lu, T.-B. Enhancing the hygroscopic stability of S-oxiracetam via pharmaceutical cocrystals. *Cryst. Growth Des.* **2012**, *12* (9), 4562−4566.
(34) Patel, V.; Akimbekov, N. S.; Grant, W. B.; Dean, C.; Fang, X.; Razzaque, M. S. Neuroprotective effects of magnesium: Implications for neuroinflammation and cognitive decline. *Front. Endocrinol.* **2024**, *15*, 1406455.
(35) Shabani, S.; Rabiei, Z.; Amini-Khoei, H. Exploring the multifaceted neuroprotective actions of gallic acid: A review. *Int. J. Food Prop.* **2020**, *23* (1), 736−752.
(36) Sheldrick, G. M. SHELXT − Integrated space-group and crystal-structure determination. *Acta Crystallogr., Sect. A: found. Adv.* **2015**, *71* (1), 3−8.
(37) Sheldrick, G. M. Crystal structure refinement with*SHELXL*. *Acta Crystallogr., Sect. C: Struct. Chem.* **2015**, *71* (1), 3−8.
(38) Dolomanov, O. V.; Bourhis, L. J.; Gildea, R. J.; Howard, J. A. K.; Puschmann, H. OLEX2: a complete structure solution, refinement and analysis program. *J. Appl. Crystallogr.* **2009**, *42* (2), 339−341.
(39) Macrae, C. F.; Sovago, I.; Cottrell, S. J.; Galek, P. T. A.; McCabe, P.; Pidcock, E.; Platings, M.; Shields, G. P.; Stevens, J. S.; Towler, M.; et al. Mercury 4.0: from visualization to analysis, design and prediction. *J. Appl. Crystallogr.* **2020**, *53* (1), 226−235.
(40) Malykh, A. G.; Sadaie, M. R. Piracetam and piracetam-like drugs. *Drugs* **2010**, *70* (3), 287−312.
(41) Gouliaev, A. H.; Senning, A. Piracetam and other structurally related nootropics. *Brain Res. Rev.* **1994**, *19* (2), 180−222.
(42) Li, W.; Liu, H.; Jiang, H.; Wang, C.; Guo, Y.; Sun, Y.; Zhao, X.; Xiong, X.; Zhang, X.; Zhang, K.; et al. (S)-Oxiracetam is the active ingredient in oxiracetam that alleviates the cognitive impairment induced by chronic cerebral hypoperfusion in rats. *Sci. Rep.* **2017**, *7* (1), 10052.
(43) Gallai, V.; Mazzotta, G.; Del Gatto, F.; Montesi, S.; Mazzetti, A.; Dominici, P.; Della Monica, A. A clinical and neurophysiological trial on nootropic drugs in patients with mental decline. *Acta Neurologica* **1991**, *13* (1), 1−12.
(44) Wouters, J.; Tilborg, A.; Quéré, L. Concluding remarks using piracetam as a learning model. In *Pharmaceutical Salts and Co-crystals*; Royal Society of Chemistry, 2012; pp. 330−337.
(45) Aitipamula, S.; Chow, P. S.; Tan, R. B. Co-crystals of caffeine and piracetam with 4-hydroxybenzoic acid: Unravelling the hidden hydrates of 1: 1 co-crystals. *CrystEngcomm* **2012**, *14* (7), 2381−2385.
(46) Braga, D.; Grepioni, F.; Maini, L.; Capucci, D.; Nanna, S.; Wouters, J.; Aerts, L.; Quéré, L. Combining piracetam and lithium salts: ionic co-crystals and co-drugs? *Chem. Commun.* **2012**, *48* (66), 8219−8221.
(47) Viertelhaus, M.; Hilfiker, R.; Blatter, F.; Neuburger, M. Piracetam co-crystals with OH-group functionalized carboxylic acids. *Cryst. Growth Des.* **2009**, *9* (5), 2220−2228.
(48) Song, L.; Robeyns, K.; Leyssens, T. Crystallizing ionic cocrystals: Structural characteristics, thermal behavior, and crystallization development of a piracetam-CaCl2 cocrystallization process. *Cryst. Growth Des.* **2018**, *18* (5), 3215−3221.
(49) Admiraal, G.; Eikelenboom, J.; Vos, A. Structures of the triclinic and monoclinic modifications of (2-oxo-1-pyrrolidinyl) acetamide. *Struct. Sci.* **1982**, *38* (10), 2600−2605.
(50) Louër, D.; Louër, M.; Dzyabchenko, V.; Agafonov, V.; Ceolin, R. Structure of a metastable phase of piracetam from X-ray powder

https://doi.org/10.1021/acs.cgd.5c00735
Cryst. Growth Des. 2025, 25, 6754−6763

diffraction using the atom−atom potential method. *Struct. Sci.* **1995**, *51* (2), 182−187.
(51) Maher, A.; Seaton, C. C.; Hudson, S.; Croker, D. M.; Rasmuson, Å. C.; Hodnett, B. K. Investigation of the solid-state polymorphic transformations of piracetam. *Cryst. Growth Des.* **2012**, *12* (12), 6223−6233.
(52) Bandoli, G.; Grassi, A.; Nicolini, M.; Pappalardo, G. C. Solid-state structure and conformation of the nootropic agent 4-hydroxy-2-oxo-1-pyrrolidineacetamide: X-ray and theoretical self-consistant field molecular orbital (SCF-MO) studies. *Chem. Pharm. Bull.* **1985**, *33* (10), 4395−4401.
(53) Shemchuk, O.; Braga, D.; Grepioni, F. Alloying barbituric and thiobarbituric acids: from solid solutions to a highly stable keto co-crystal form. *Chem. Commun.* **2016**, *52* (79), 11815−11818.
(54) Chen, A.; Cai, P.; Luo, M.; Guo, M.; Cai, T. Melt crystallization of celecoxib-carbamazepine cocrystals with the synchronized release of drugs. *Pharm. Res.* **2023**, *40* (2), 567−577.
(55) Yan, Y.; Chen, J.-M.; Lu, T.-B. Thermodynamics and preliminary pharmaceutical characterization of a melatonin−pimelic acid cocrystal prepared by a melt crystallization method. *CrystEngcomm* **2015**, *17* (3), 612−620.
(56) Khoj, M. A.; Hughes, C. E.; Harris, K. D.; Kariuki, B. M. Structural diversity of solid solutions formed between 3-chloro-trans-cinnamic acid and 3-bromo-trans-cinnamic acid. *Cryst. Growth Des.* **2017**, *17* (3), 1276−1284.
(57) Song, L.; Leng, F.; Robeyns, K.; Leyssens, T. Quaternary phase diagrams as a tool for ionic cocrystallization: the case of a solid solution between a racemic and enantiopure ionic cocrystal. *CrystEngcomm* **2020**, *22* (14), 2537−2542.
(58) Bajpai, A.; Scott, H. S.; Pham, T.; Chen, K.-J.; Space, B.; Lusi, M.; Perry, M. L.; Zaworotko, M. J. Towards an understanding of the propensity for crystalline hydrate formation by molecular compounds. *IUCrJ.* **2016**, *3* (6), 430−439.
(59) Infantes, L.; Fábián, L.; Motherwell, W. S. Organic crystal hydrates: what are the important factors for formation. *CrystEngcomm* **2007**, *9* (1), 65−71.
(60) Bazzini, P.; Wermuth, C.; Wermuth, C.; Aldous, D.; Raboisson, P.; Rognan, D. Chapter 13—Substituent Groups. *Practice Of Medicinal Chemistry*; Academic Press, 2008.
(61) Rosi, D.; Peruzzotti, G.; Dennis, E.; Berberian, D.; Freele, H.; Archer, S. A new, active metabolite of 'Miracil D'. *Nature* **1965**, *208* (5014), 1005−1006.
(62) Cappelli, A.; Giuliani, G.; Pericot Mohr, G. L.; Gallelli, A.; Anzini, M.; Vomero, S.; Cupello, A.; Scarrone, S.; Matarrese, M.; Moresco, R. M.; et al. A non-peptide NK1 receptor agonist showing subpicomolar affinity. *J. Med. Chem.* **2004**, *47* (6), 1315−1318.
(63) Florez, D. H. Â.; dos Santos Moreira, A. M.; da Silva, P. R.; Brandão, R.; Borges, M. M. C.; de Santana, F. J. M.; Borges, K. B. Desomorphine (Krokodil): An overview of its chemistry, pharmacology, metabolism, toxicology and analysis. *Drug Alcohol Depen.* **2017**, *173*, 59−68.

https://doi.org/10.1021/acs.cgd.5c00735
Cryst. Growth Des. 2025, 25, 6754−6763